Journal of Mechanisms and Robotics. Received August 14, 2024;
Accepted manuscript posted October 06, 2024. doi:10.1115/1.4066850

The Synthesis of Spherical Four-bars for Biomimetic Motion through Complete Solutions for Approximate Rigid Body Guidance

Sam O'Connor
Mark Plecnik*
University of Notre Dame
Department of Aerospace and Mechanical Engineering
Notre Dame, IN 46556
Email: {soconn22, plecnikmark}@nd.edu

In this paper, we form a constrained optimization problem for spherical four-bar motion generation. Instead of using local optimization methods, all critical points are found using homotopy continuation solvers. The complete solution set provides a full view of the optimization landscape and gives the designer more freedom in selecting a mechanism. The motion generation problem admits 61 critical points, of which two must be selected for each four-bar mechanism. We sort solutions by objective value and perform a second order analysis to determine if the solution is a minimum, maximum, or saddle point. We apply our approximate synthesis technique to two applications: a hummingbird wing mechanism and a sea turtle flipper gait. Suitable mechanisms were selected from the respective solution sets and used to build physical prototypes.
Keywords: spherical kinematics, optimization, synthesis

1 Introduction

The spherical four-bar is a four-link mechanism with four revolute joints, whose axes intersect at a common point. Motion generation for the spherical four-bar, also known as rigid body guidance, involves synthesizing the mechanism dimensions that produce a desired coupler link motion. The coupler link motion is fully defined by its orientation. The position of the point on the coupler that is coincident with the intersection point of the joint axes is fully constrained, so all motion of the body is a pure rotation. Equivalently, a point on the coupler at some fixed radius from the intersection point produces a motion on a spherical surface. The motion of the spherical four-bar is independent to radial scaling, which makes it useful for producing spatial motions. In this paper, we formulate the approximate motion generation of spherical four-bars with an optimization procedure that produces all optimal solutions.

Exact synthesis is a common approach to kinematic design, where all desired task orientations are met exactly. This method has been well-studied for the spherical four-bar and has been solved in its completeness for three orientations [1], four orientations [2], and a maximum of five orientations [3]. Specifying more than five coupler orientations results in an over-defined system, so approximate synthesis approaches must be used instead. Generally, this involves forming an objective function that minimizes the error between the optimal mechanism and the desired task orientations. Alizade et. al. [4] formed a least-square optimization that resulted in a fourth-order polynomial. The nonlinear equation was converted to a system of linear equations with nonlinear operators and solved for up to four real solutions. Li et. al. [5] developed a kinematic mapping approach to spherical motion generation and solved a least-squares fitting with singular value decomposition. Liu et. al. [6] solved the optimization problem using a genetic algorithm. To ensure optimal solutions were found, the algorithm was repeated hundreds of times with a randomized initial population. In a different approach, Sun et. al. [7] used the harmonic output parameters of the spherical four-bar to develop a numerical atlas. This method avoids computing roots to nonlinear equations, but requires time for the algorithm to search a pre-constructed atlas for possible solutions.

In our method, we form a constrained optimization problem to approximate a desired set of task orientations. We derive the first-order necessary conditions, which form a square system of polynomials. The discrete task orientation data from the objective function is fully contained within the coefficients of these polynomials, so their algebraic form is invariant to the number of end-effector orientations specified. Instead of using a local optimization method, we compute all critical points by finding the roots of the polynomial system using the homotopy continuation solver Bertini [8]. These points are classified as maxima, minima, or saddle points through a second-order analysis, and their principal directions of curvature are also computed. This work provides

*Address all correspondence to this author.

Journal of Mechanisms and Robotics. Received August 14, 2024;
Accepted manuscript posted October 06, 2024. doi:10.1115/1.4066850

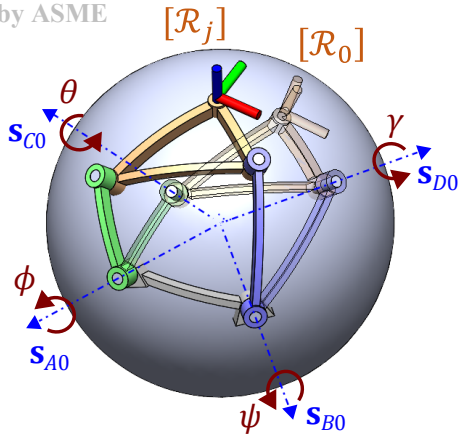

Fig. 1. Kinematic diagram of the spherical four-bar linkage

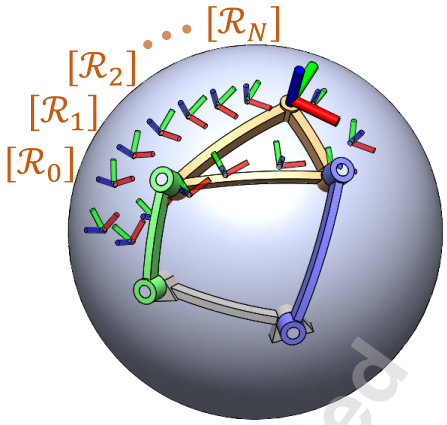

Fig. 2. Task orientation specification

the designer with many solution options and a full view of the optimization space, which is ideal for *design exploration*. Unlike other local search methods, which are better for *design tuning*, a nearby initial guess is not required to locate all minima. Other work [9] has shown saddle points to be useful in mapping connections between minima in the design space. This paper is related to our previous work [10], in which a similar method was applied to spherical four-bar function generators.

In Sect. 2, we formulate the kinematic constraints for a spherical four-bar. In Sect. 3, we formulate an optimization problem to compute a complete solution set for approximate synthesis and classify solutions for efficient design exploration. In Sect. 4, we apply our approximate synthesis method to recreate the flapping motion of a hummingbird and the walking gait of a sea turtle. Conclusions are offered in Sect. 5.

2 Motion Generation Set-Up

A kinematic diagram of the spherical four-bar is shown in Fig. 1. The mechanism dimensions are specified using the directions of the four joint axes and the orientation of the coupler link in a reference configuration. The ground pivots are denoted $\mathbf{s}_{A0}$ and $\mathbf{s}_{B0}$, and the moving pivots are denoted by $\mathbf{s}_{C0}$ and $\mathbf{s}_{D0}$. The orientation of the coupler link is given using a 3×3 rotation matrix $[\mathcal{R}_0]$. Rotations about the ground pivots $\mathbf{s}_{A0}$ and $\mathbf{s}_{B0}$ are parameterized by ϕ and ψ, respectively. Relative rotations between neighboring links at the moving pivots $\mathbf{s}_{C0}$ and $\mathbf{s}_{D0}$ are parameterized by θ and ρ, respectively. The rotation matrix $[\mathcal{R}(\mathbf{s},\phi)]$ rotates a vector or another rotation matrix by an angle ϕ about unit vector $\mathbf{s}$, where

$$[\mathcal{R}(\mathbf{s},\phi)] = [I] + \sin\phi[\tilde{s}] + (1-\cos\phi)[\tilde{s}]^2, \qquad (1)$$

$$\text{where } \mathbf{s} = \begin{Bmatrix} s_x \\ s_y \\ s_z \end{Bmatrix}, \quad \text{and } [\tilde{s}] := \begin{bmatrix} 0 & -s_z & s_y \\ s_z & 0 & -s_x \\ -s_y & s_x & 0 \end{bmatrix}.$$

The displaced orientation of the coupler, $[\mathcal{R}_j]$, for angles ϕ_j, ψ_j, θ_j, and ρ_j, is expressed by splitting the mechanism into two 2R chains and rotating the home orientation using the rotation matrices in Eq. (1),

$$[\mathcal{R}_j] = [\mathcal{R}(\mathbf{s}_{A0},\phi_j)][\mathcal{R}(\mathbf{s}_{C0},\theta_j)][\mathcal{R}_0], \qquad (2)$$
$$[\mathcal{R}_j] = [\mathcal{R}(\mathbf{s}_{B0},\psi_j)][\mathcal{R}(\mathbf{s}_{D0},\rho_j)][\mathcal{R}_0]. \qquad (3)$$

The goal of motion generation is to find the reference joint axes $\mathbf{s}_{A0}$, $\mathbf{s}_{B0}$, $\mathbf{s}_{C0}$, and $\mathbf{s}_{D0}$ that achieve N specified task orientations, $[\hat{\mathcal{R}}_j], j = 0,1,\ldots,N-1$, as shown in Fig. 2.

Without loss of generality, any set of task orientations may begin with $[\mathcal{R}_0] = [I]$, where $[I]$ is the 3×3 identity matrix. In case $[\mathcal{R}_0]$ is not set as identity, task orientations should be transformed by $[\hat{\mathcal{R}}_0]^T$,

$$[\mathcal{R}_0] = [\hat{\mathcal{R}}_0]^T[\hat{\mathcal{R}}_0] = [I], \qquad (4)$$
$$[\mathcal{R}_j] = [\hat{\mathcal{R}}_0]^T[\hat{\mathcal{R}}_j]. \qquad (5)$$

After solving for the joint axes, we pre-multiply $\mathbf{s}_{A0}$, $\mathbf{s}_{B0}$, $\mathbf{s}_{C0}$, and $\mathbf{s}_{D0}$ by $[\hat{\mathcal{R}}_0]$ to match the original task.

Substituting Eq. (4) into Eqs. (2) and (3),

$$[\mathcal{R}_j] = [\mathcal{R}(\mathbf{s}_{A0},\phi_j)][\mathcal{R}(\mathbf{s}_{C0},\theta_j)], \qquad (6)$$
$$[\mathcal{R}_j] = [\mathcal{R}(\mathbf{s}_{B0},\psi_j)][\mathcal{R}(\mathbf{s}_{D0},\rho_j)]. \qquad (7)$$

To form the kinematic constraints, the intermediate variables ϕ_j, ψ_j, θ_j, and ρ_j must be eliminated from Eqs. (6) and (7). Starting with Eq. (6), we multiply by $\mathbf{s}_{C0}$,

$$[\mathcal{R}_j]\mathbf{s}_{C0} = [\mathcal{R}(\mathbf{s}_{A0},\phi_j)][\mathcal{R}(\mathbf{s}_{C0},\theta_j)]\mathbf{s}_{C0}. \qquad (8)$$

Rotation of a vector about itself yields the same vector, so

$$[\mathcal{R}_j]\mathbf{s}_{C0} = [\mathcal{R}(\mathbf{s}_{A0},\phi_j)]\mathbf{s}_{C0}. \qquad (9)$$

Take the dot product of both sides with $\mathbf{s}_{A0}$ and rearrange the order of multiplication in the dot product on the right hand side,

$$([\mathcal{R}_j]\mathbf{s}_{C0}) \cdot \mathbf{s}_{A0} = ([\mathcal{R}(\mathbf{s}_{A0}, \phi_j)]\mathbf{s}_{C0}) \cdot \mathbf{s}_{A0}, \tag{10}$$

$$= \mathbf{s}_{C0} \cdot ([\mathcal{R}(\mathbf{s}_{A0}, \phi_j)]^T \mathbf{s}_{A0}). \tag{11}$$

Here once again, $\mathbf{s}_{A0}$ is stationary after rotation about its own axis. Simplifying and rearranging, the kinematic constraint for the $\mathbf{s}_{A0}$ side becomes

$$\mathbf{s}_{A0} \cdot ([\mathcal{R}_j]\mathbf{s}_{C0}) = \mathbf{s}_{A0} \cdot \mathbf{s}_{C0}. \tag{12}$$

The same approach can be used for Eq. (7), yielding the constraint on the $\mathbf{s}_{B0}$ side,

$$\mathbf{s}_{B0} \cdot ([\mathcal{R}_j]\mathbf{s}_{D0}) = \mathbf{s}_{B0} \cdot \mathbf{s}_{D0}. \tag{13}$$

These kinematic constraints have the same algebraic form, i.e. any $\mathbf{s}_{A0}$ and $\mathbf{s}_{C0}$ that satisfy Eq. (12) would also satisfy Eq. (13) for $\mathbf{s}_{B0}$ and $\mathbf{s}_{D0}$. This decouples the problem into two identical 2R synthesis problems. Therefore, Eq. (12) can be solved once, and solutions can be selected for each side.

3 Optimization Formulation

Instead of satisfying Eq. (12) exactly at each task orientation, our goal is to approximately meet the specified coupler orientations. We choose N task orientations and modify our constraint from Eq. (12) to form kinematic constraint residuals,

$$\eta_j := \mathbf{s}_{A0} \cdot [\mathcal{R}_j]\mathbf{s}_{C0} - R_{AC} \qquad j = 0, 1, \ldots, N-1.$$

We introduced a new variable R_{AC}, which acts as a best-fit link dimension approximately equal to $\mathbf{s}_{A0} \cdot \mathbf{s}_{C0}$. We choose one task orientation to be the reference configuration, $[\hat{\mathcal{R}}_0]$, and multiply all task orientations by its transpose, as described in Sect. 2. We also define quadratic sphere constraints to make $\mathbf{s}_{A0}$ and $\mathbf{s}_{C0}$ unit vectors,

$$\mathbf{s}_{A0} \cdot \mathbf{s}_{A0} = 1 \qquad \text{and} \qquad \mathbf{s}_{C0} \cdot \mathbf{s}_{C0} = 1. \tag{14}$$

The objective of our optimization is to minimize the sum of squares of the kinematic constraint residuals, η_j,

$$\min_{\mathbf{s}_{A0},\, \mathbf{s}_{C0},\, R_{AC}} \quad f := \frac{1}{2} \sum_{j=0}^{N-1} \eta_j^2 \tag{15}$$

$$\text{s.t.} \quad \mathbf{h} := \begin{Bmatrix} \mathbf{s}_{A0} \cdot \mathbf{s}_{A0} - 1 \\ \mathbf{s}_{C0} \cdot \mathbf{s}_{C0} - 1 \end{Bmatrix} = 0.$$

The corresponding Lagrangian is

$$\mathcal{L} := \tfrac{1}{2} \sum_{j=0}^{N-1} \eta_j^2 + \mathbf{h}^T \boldsymbol{\lambda}, \tag{16}$$

where $\boldsymbol{\lambda} = \{\lambda_1,\ \lambda_2\}$ are Lagrange multipliers.

We define the decision variables, $\mathbf{x}$, as the vector components of $\mathbf{s}_{A0}$ and $\mathbf{s}_{C0}$ and the variable R_{AC}. We form the first-order necessary conditions by taking the partial derivatives of Eq. (16) with respect to $\mathbf{x}$ and $\boldsymbol{\lambda}$,

$$\frac{\partial \mathcal{L}}{\partial \mathbf{x}} = 0 \tag{17}$$

$$\frac{\partial \mathcal{L}}{\partial \boldsymbol{\lambda}} = \mathbf{h} = 0. \tag{18}$$

Eqs. (17) and (18) form a system of nine polynomials in nine variables. The roots of this system are the critical points of the optimization problem.

3.1 Computational Results

The discrete task orientation data is contained within the coefficients of Eqs. (17) and (18). As a result, the algebraic structure is invariant to the number of task orientations specified. A 3-homogenous grouping partitioned by the components of $\mathbf{s}_{A0}$, the components of $\mathbf{s}_{C0}$, and the group $\{R_{AC}, \lambda_1, \lambda_2\}$ indicates a Bézout degree of 3564 for the system. The polynomial homotopy continuation solver Bertini found 244 finite, isolated solutions. Further analysis shows these solutions occur in sets of four. Namely, for every solution $\{\mathbf{s}_{A0}, \mathbf{s}_{C0}\}$, the solutions $\{\mathbf{s}_{A0}, -\mathbf{s}_{C0}\}$, $\{-\mathbf{s}_{A0}, -\mathbf{s}_{C0}\}$, and $\{-\mathbf{s}_{A0}, \mathbf{s}_{C0}\}$ also exist. This is a result of the quadratic sphere constraints. Each solution in the set of four produces the same motion, so only one copy is kept. The system can then be computed using a parameter homotopy that only needs to track 61 paths. Proceeding computations take roughly 5 seconds on a personal computer for any set of task orientations.

Once solutions are computed, complex solutions are removed. Each solution is only half of the four-bar, so two solutions must be selected for each possible mechanism. For M real solutions, there exist M choose 2 solution combinations. Empirically, the number of real solutions ranges from 10-30, resulting in anywhere from 50-400 possible mechanisms. To efficiently parse and select mechanisms, each solution is plugged back into the objective of Eq. (15). For each mechanism, the objective values of each of the two solutions are added together, and the mechanisms are sorted from lowest to highest total objective value.

3.2 Eigenanalysis of Critical Points

Both minima and saddles are computed in our complete solution set to provide a full picture of the design space. Saddle points have utility for other downstream design activities, like mapping connections between minima [9]. Computing

the complete solution set is particularly advantageous for this problem, since two solutions need to be selected to construct each four-bar. A local optimization method would require randomizing initial guesses until the solver converged to two different minima.

To identify each critical point as a minimum, maximum, or saddle point, we compute the eigenvalues and eigenvectors of the *projected Hessian*, which is appropriate for equality-constrained optimization. Recalling Eqs. (15)-(18), the Hessian $[\mathcal{H}(\mathbf{x})] = \left[\frac{\partial^2 f}{\partial \mathbf{x}^2}\right]$ is a 7×7 matrix. The derivative $\left[\frac{\partial \mathbf{h}}{\partial \mathbf{x}}\right]$ is a 2×7 matrix with row vectors that span the space normal to the constraints. The null space of $\left[\frac{\partial \mathbf{h}}{\partial \mathbf{x}}\right]$ contains the 5 basis vectors of the tangent space. We orthonormalize these vectors and place them in $[T]$, a 7×5 matrix. We then compute the projected Hessian, $[T]^T[\mathcal{H}(\mathbf{a})][T]$, a 5×5 matrix. The eigenvectors of this matrix indicate the principal directions of curvature after transformation by $[T]$, and the eigenvalues are the principal curvatures. Positive eigenvalues indicate directions of ascent, and negative eigenvalues indicate directions of descent. If all eigenvalues are positive or all eigenvalues are negative, the point is a minimum or maximum, respectively. Other points are saddle points, which are classified as index-k saddles if k eigenvalues are negative. Other work [9] has shown the usefulness of characterizing descent directions.

3.3 Error calculation

As a metric to validate the effectiveness of designs, the error was computed between the specified task orientations and the actual motion of each solution. Given the four-bar dimensions of a solution, $\{\mathbf{s}_{A0}, \mathbf{s}_{B0}, \mathbf{s}_{C0}, \mathbf{s}_{D0}\}$, orientations of the coupler link were sampled, $[\mathcal{R}_k]$, $k = 1, ..., 1000$, using the mechanism's forward kinematics. For each specified task orientation, $[\mathcal{R}_j]$, $j = 1, ..., N$, the orientation on the mechanism's coupler that was nearest to the specified task orientation was compared.

The relative rotation between $[\mathcal{R}_j]$ and $[\mathcal{R}_k]$ is

$$[\mathcal{R}_{jk}] = [\mathcal{R}_j]^T[\mathcal{R}_k]. \tag{19}$$

Considering axis-angle parameters, the angle of $[\mathcal{R}_{jk}]$ is

$$\varphi_{jk} = \arccos\left(\tfrac{1}{2}(\text{tr}[\mathcal{R}_{jk}] - 1)\right). \tag{20}$$

Note that $\varphi_{jk} \in [0, \pi]$. To measure the difference between $[\mathcal{R}_j]$ and $[\mathcal{R}_k]$, we use the formula,

$$\epsilon_{jk} = 1 - \cos\frac{\varphi_{jk}}{2}, \tag{21}$$

where $\epsilon_{jk} \in [0, 1]$ with the lower bound indicating that $[\mathcal{R}_j]$ and $[\mathcal{R}_k]$ are the same. The nearness of the j^{th} task orientation to the coupler's motion is computed by taking the minimum from its discretized motion,

$$\epsilon_j = \min\left(\{\epsilon_{jk}\}_{k=1}^{1000}\right). \tag{22}$$

The error between a set of task orientations and a coupler motion is then

$$\epsilon = \frac{1}{N}\sum_{j=0}^{N-1}\epsilon_j. \tag{23}$$

This error metric was computed between the set of task orientations and every continuous motion branch of a single four-bar. The motion branch which yielded the least error was used as the metric for that four-bar. In this way, branch defects are accounted for. We use this error metric to evaluate solutions, and we compare it to the objective values of our solutions in Sec. 4.1

4 Applications

Many spatial motions can be well-approximated as one degree-of-freedom spherical motions. We applied our approximate synthesis method to two bioinspired motions: the flapping of a hummingbird wing and the walking motion of a sea turtle.

4.1 Hummingbird Wing Flapping

One example of a spatial motion that is nearly spherical in nature is the flapping of a hummingbird's wings. Unlike most birds, hummingbirds are able to hover and maneuver quickly due to their wing flapping. Instead of only producing lift during the downstroke of the flapping motion, they twist their wings to produce lift on the upstroke as well [11]. This results in a figure-8 motion that can be well-approximated as spherical. Rehmat et. al. [12] discovered a spherical four-bar with hummingbird-like motion from a family of mechanisms with symmetric coupler curves. McDonald and Agrawal [13] designed a similar spherical four-bar for a flapping micro air-vehicle application using a local optimization method. Here, we apply our approximate synthesis method to find a mechanism that replicates the flapping of a hummingbird wing.

We specify task orientations with the Euler angles α_1, α_2, and α_3, which produce the orientation

$$[\mathcal{R}_j] = [Y(\alpha_{1,j})][X(\alpha_{2,j})][Z(\alpha_{3,j})], \quad j = 0, \ldots, N-1 \tag{24}$$

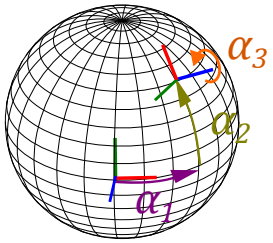

Fig. 3. Euler angle parameterization

where $[X(\alpha_1)]$, $[Y(\alpha_2)]$, and $[Z(\alpha_3)]$ are the rotations about fixed axes x, y, and z. This Euler angle specification corresponds to the longitude α_1 and latitude $-\alpha_2$, which locate the task orientation on a spherical surface, and the rotation angle α_3, which rotates the task orientation about the axis normal to the spherical surface. This is shown in Fig. 3. We found this Euler angle parameterization to be convenient, but any other rotation matrix parameterization could similarly be used to specify task orientations.

To reproduce the hummingbird wing motion, we manually specified 15 orientations, which are tabulated in Table 1 and shown in Fig. 4. These task orientations trace a figure-eight on the surface of a sphere. The rotation angles of each task orientation about the axis normal to the sphere were chosen such that the wings are always angled down during the forward and backward strokes. We applied our optimization procedure and computed all critical points. Of the 61 critical points, 21 were real, which resulted in 210 possible mechanisms after enumerating combinations. The mechanisms were ordered from least to greatest by the summation of the objectives of their two component critical points. The mechanisms with the 12 lowest objective values are shown in Fig. 5.

Solutions were parsed to find a suitable mechanism for the wing application. Several mechanisms had defects, where the motion was split into two circuits or branches by a singularity. Mechanism 11 completes the entire figure-eight motion without encountering singularities and approximates the task orientations very closely, so it was chosen for this application. While it may seem unexpected that the 11th-highest objective value would be preferred over the global minima or other solutions with lower objective value, it satisfied design criteria that the objective did not capture, such as avoiding defects and having suitable ground pivot locations. Mechanism 11 is composed of a minimum and a saddle point, yet its objective value is still within 0.03 of the global minimum.

The error of each solution, defined in Sec. 3.3, is also included in Fig. 5. To compare the abilities of our objective value and error metric to sort desirable solutions, we plot the error against the objective value in Fig. 6. The relationship

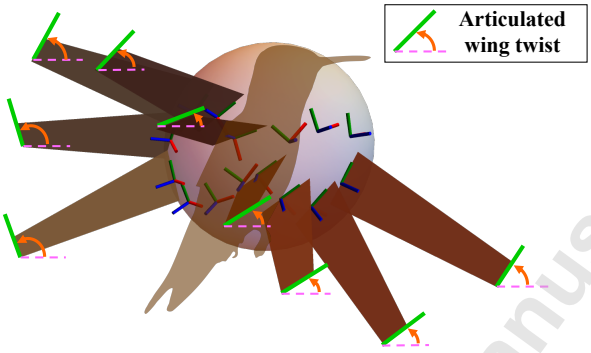

Fig. 4. Visualization of task orientations for hummingbird flapping

Table 1. Task orientations for hummingbird flapping motion

j	$\alpha_1[^\circ]$	$\alpha_2[^\circ]$	$\alpha_3[^\circ]$
1	30.94	18.33	−30.60
2	−41.83	−25.21	−22.00
3	−24.64	−25.21	−42.28
4	−53.29	13.18	6.07
5	16.04	−15.47	49.56
6	13.75	13.18	−47.10
7	−42.40	23.49	3.38
8	−12.03	−16.04	−65.20
9	1.15	1.15	−49.39
10	−58.44	−8.02	−19.31
11	30.94	−20.05	14.15
12	−20.63	18.33	27.56
13	51.57	−16.04	0.00
14	−5.73	5.16	57.30
15	46.41	6.88	−24.12

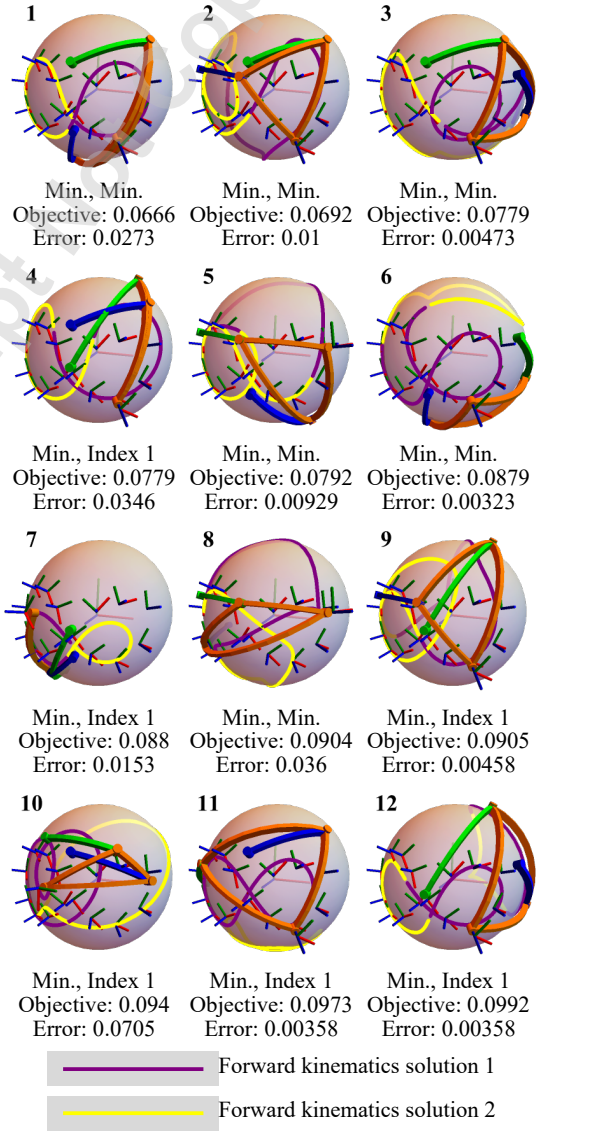

Fig. 5. Mechanisms with the the lowest objective value for hummingbird flapping

Journal of Mechanisms and Robotics. Received August 14, 2024;
Accepted manuscript posted October 06, 2024. doi:10.1115/1.4066850

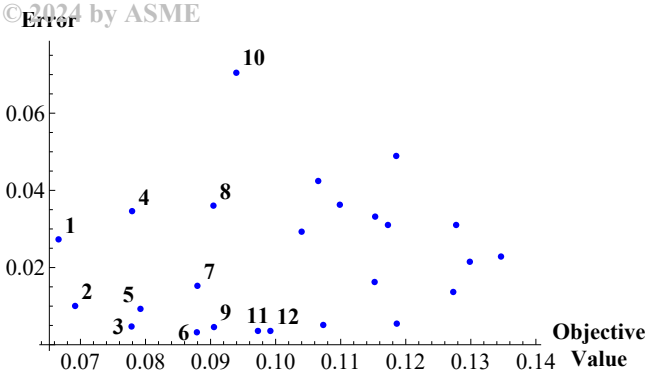

Fig. 6. Error vs. objective value for the 25 mechanisms with the smallest objective value for hummingbird flapping. Mechanisms shown in Fig. 5 are labeled.

between error and objective value is not monotonic. There are many solutions with low objective values that have higher error than solutions with high objective values. For example, solution 11 has a higher objective value than solution 4, but about half of the error. The discrepancy between error and objective value comes from the decoupling of the synthesis procedure into two 2R linkages. The objective value only considers the ability of a 2R to meet the task orientations, so summing the objectives of two 2R solutions into a four-bar mechanism could yield less favorable designs with low objective values. Alternatively, the error metric gives information on the performance of the full four-bar mechanism, so it aligns more closely with what a designer would consider "good" designs. A prototype of this mechanism was constructed and is shown in Figs. 7 and 8.

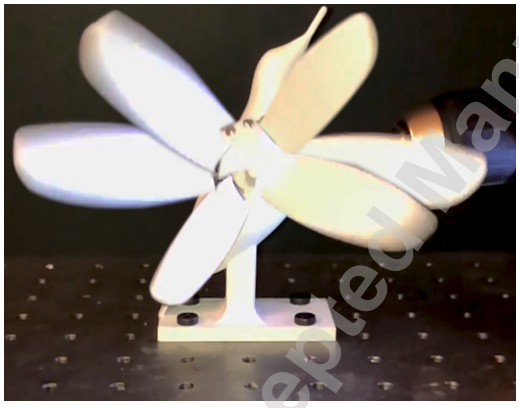

Fig. 7. Hummingbird wing flapping prototype

4.2 Sea Turtle Walking

A robotic sea turtle was developed similar to [14]. This robot mimics the way the turtle traverses difficult terrain like rocks and sand. The motion of the sea turtle's front flippers propel its body across granular media. We studied these motions and applied our synthesis method to find a mechanism that approximates the motion.

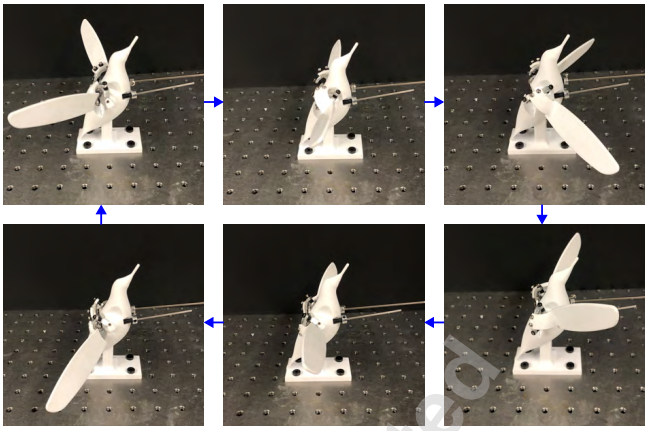

Fig. 8. Hummingbird wing orientations

Fifteen task orientations were manually chosen for the turtle flipper motion, using the same Euler angle parameterization as Sect. 4.1. The task orientations are listed in Table 2 and shown in Fig. 9. In the bottom portion of the stroke, the flipper is nearly vertical, which helps it push through granular media. On the return part of the stroke, the flipper flattens out and reaches forward to prepare for the next stroke. We computed all solutions for these task orientations using our approximate synthesis technique. From the 61 critical points, 13 were real. This resulted in 78 mechanisms. Mechanisms

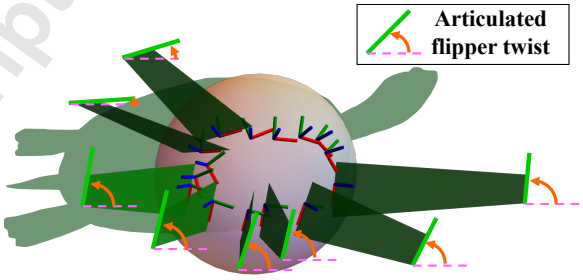

Fig. 9. Visualization of task orientations for turtle walking

Table 2. Task orientations for turtle walking motion

j	$\alpha_1[^\circ]$	$\alpha_2[^\circ]$	$\alpha_3[^\circ]$
1	1.72	−30.94	25.61
2	−15.18	2.29	−100.90
3	14.90	−30.94	−5.39
4	30.65	−31.51	−19.37
5	32.37	2.29	−103.71
6	11.46	2.29	−95.17
7	−26.64	−8.59	−62.51
8	−20.63	−15.47	−48.36
9	41.54	−29.22	−51.34
10	−26.07	−21.77	9.91
11	3.44	5.73	−100.90
12	−28.93	−4.01	−97.92
13	−16.90	−30.94	22.80
14	46.12	−22.35	−61.94
15	50.99	−5.73	−94.31

Journal of Mechanisms and Robotics. Received August 14, 2024;
Accepted manuscript posted October 06, 2024. doi:10.1115/1.4066850

were ordered by objective value. The 12 mechanisms with the lowest objective values are shown in Fig. 10.

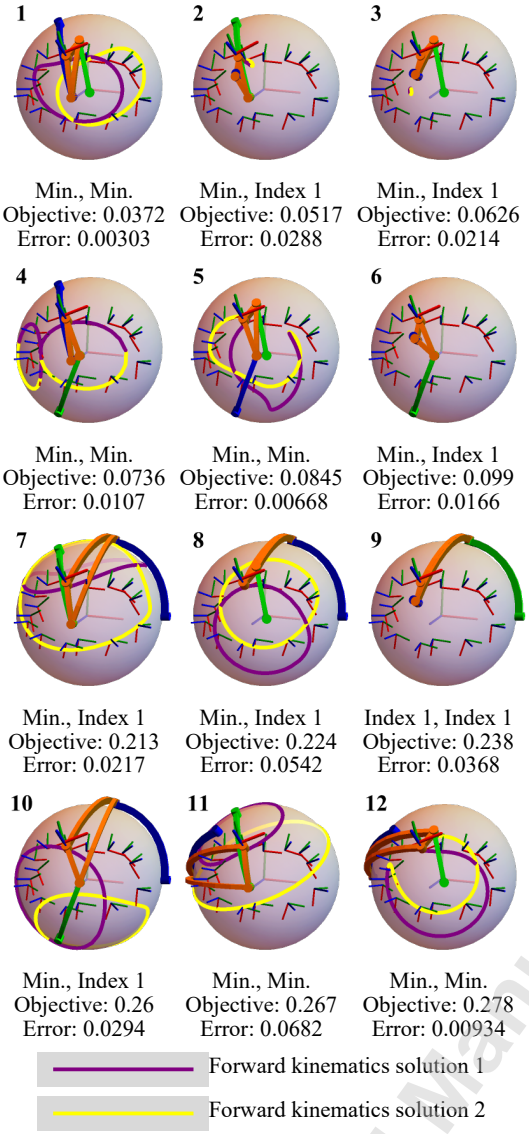

Fig. 10. Mechanisms with the the lowest objective value for turtle walking

Unlike the hummingbird wing, Mechanism 1 was free of defects and approximated the specified motion very closely. Additionally, both solutions were local minima. The mechanism was implemented in a sea turtle robot, shown in Fig. 11. Mechanisms 2, 3, 6, and 9 produce nearly no motion, yet they have very low objective values. These mechanisms are degenerate solutions, where the $\mathbf{s}_{B0}$ and $\mathbf{s}_{D0}$ vectors are nearly coincident. The degenerate 2R solution can only produce a one degree-of-freedom motion in a circle about the two coincident axes. Since the turtle motion is nearly circular, it is not surprising that this solution would have a low objective value. However, once paired with another solution to form a full four-bar, the mechanism loses its mobility due to the degeneracy. This is made clear by the high error values for these degenerate solutions. Fortunately, with the complete set of optimal mechanisms, these solutions can simply be discarded.

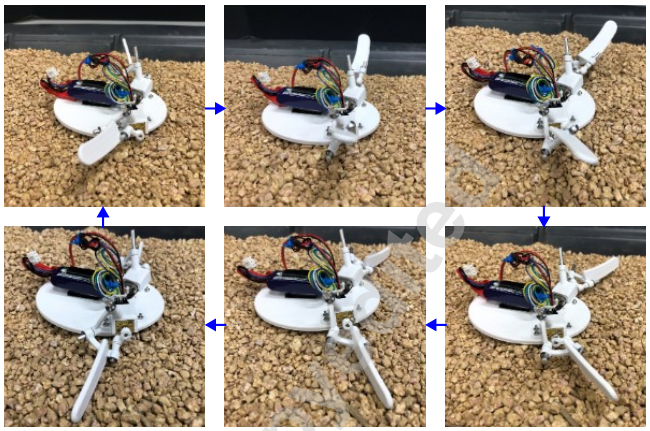

Fig. 11. Turtle robot prototype

5 Conclusion

In our approach to the approximate motion generation of spherical four-bars, we compute all critical points to a nonlinear optimization problem. Instead of using local search methods, which require initialization near the local minima, we obtain all minima and saddle points to give the designer a full view of the design space. For the general case of motion generation for spherical four-bars, our method computes all 61 sets of critical points and sorts them to find the most useful designs. We demonstrated our method with the design of a hummingbird wing-flapping mechanism and a sea turtle walking robot. We obtained 210 possible mechanisms for the hummingbird wing and 78 possible mechanisms for the sea turtle robot. We selected suitable designs from each solution set and validated their functionality with physical prototypes.

Acknowledgment

We thank Nandini Sadagopan for inspiration on the hummingbird design. We thank Dr. Yasemin Ozkan-Aydin and Nnamdi Chikere for inspiration on the sea turtle design. This material is based upon work supported by the National Science Foundation under Grant No. CMMI-2144732. This paper was presented at the 2024 International Design Engineering Technical Conferences & Computers and Information in Engineering Conference (IDETC-CIE2024).

References

[1] Bagci, C., 1984. "Geometric methods for the synthesis of spherical mechanisms for the generation of functions, paths and rigid-body positions using conformal

projections". *Mechanism and Machine Theory,* **19**(1), Jan., pp. 113–127.

[2] Ruth, D. A., and McCarthy, J. M., 1999. "The design of spherical 4R linkages for four specified orientations". *Mechanism and Machine Theory,* **34**(5), July, pp. 677–692.

[3] Lin, C.-C., 1998. "Complete Solution of the Five-Position Synthesis for Spherical Four-Bar Mechanisms". *Journal of Marine Science and Technology,* **6**(1), June.

[4] Alizade, R., Can, F. C., and Kilit, , 2013. "Least square approximate motion generation synthesis of spherical linkages by using Chebyshev and equal spacing". *Mechanism and Machine Theory,* **61**, Mar., pp. 123–135.

[5] Li, X., Zhao, P., Purwar, A., and Ge, Q. J., 2017. "A Unified Approach to Exact and Approximate Motion Synthesis of Spherical Four-Bar Linkages Via Kinematic Mapping". *Journal of Mechanisms and Robotics,* **10**(011003), Dec.

[6] Liu, W., Si, H., Wang, C., Sun, J., and Qin, T., 2023. "Dimensional synthesis of motion generation in a spherical four-bar mechanism". *Transactions of the Canadian Society for Mechanical Engineering*, Nov. Publisher: NRC Research Press.

[7] Sun, J., Chen, L., and Chu, J., 2016. "Motion generation of spherical four-bar mechanism using harmonic characteristic parameters". *Mechanism and Machine Theory,* **95**, Jan., pp. 76–92.

[8] Bates, D. J., Hauenstein, J. D., Sommese, A. J., and Wampler, C. W., 2006. Bertini: Software for numerical algebraic geometry.

[9] Baskar, A., Plecnik, M., and Hauenstein, J. D., 2022. "Computing saddle graphs via homotopy continuation for the approximate synthesis of mechanisms". *Mechanism and Machine Theory,* **176**, Oct., p. 104932.

[10] O'Connor, S., Plecnik, M., Baskar, A., and Joo, J., 2023. "Complete Solutions for the Approximate Synthesis of Spherical Four-Bar Function Generators". American Society of Mechanical Engineers Digital Collection.

[11] Yong, E., 2011. "Hummingbird flight has a clever twist". *Nature*, Dec. Publisher: Nature Publishing Group.

[12] Rehmat, Z., Roll, J., Lee, J. S., Yim, W., and Trabia, M. B., 2010. "Design of "Figure-8" Spherical Motion Flapping Wing for Miniature UAV". American Society of Mechanical Engineers Digital Collection, pp. 539–546.

[13] McDonald, M., and Agrawal, S. K., 2010. "Design of a Bio-Inspired Spherical Four-Bar Mechanism for Flapping-Wing Micro Air-Vehicle Applications". *Journal of Mechanisms and Robotics,* **2**(021012), May.

[14] Cruise, K., 2023. Robotic sea turtle mimics uniquely adaptable gait, Aug.

Figure captions and table headings